Published in "Geochemistry, Geophysics, Geosystems 17(7): 2922–2939, 2016"
which should be cited to refer to this work.

Multiscale approach to (micro)porosity quantification in continental spring carbonate facies: Case study from the Cakmak quarry (Denizli, Turkey)

Eva De Boever[1,2], Anneleen Foubert[1], Dirk Oligschlaeger[3], Steven Claes[2], Jeroen Soete[2], Pieter Bertier[4], Mehmet Özkul[5], Aurélien Virgone[6], and Rudy Swennen[2]

[1]Department of Geosciences, University of Fribourg, Fribourg, Switzerland, [2]Department of Earth and Environmental Sciences, KU Leuven, Leuven, Belgium, [3]Institut für Technische und Makromolekulare Chemie, RWTH Aachen University, Aachen, Germany, [4]Clay and Interface Mineralogy, Energy and Mineral Resources Group, RWTH Aachen, Aachen, Germany, [5]Geological Engineering, Pamukkale University, Denizli, Turkey, [6]TOTAL E&P Recherche Développement, Paris, France

Key Points:
- An approach of advanced petrophysical and imaging techniques investigating 3-D pore networks in travertine facies
- NMR T_2 distributions display a single group of micro-sized pore bodies, making up between 6 and 33% of the pore space
- The pore network of 3 travertine facies is distinctive in microporosity%, micro- to macropore connectivity and degree of heterogeneity

Supporting Information:
- Supporting Information S1

Correspondence to:
E. De Boever,
eva.deboever@unifr.ch

Abstract Carbonate spring deposits gained renewed interest as potential contributors to subsurface reservoirs and as continental archives of environmental changes. In contrast to their fabrics, petrophysical characteristics – and especially the importance of microporosity ($< 1\mu m$) – are less understood. This study presents the combination of advanced petrophysical and imaging techniques to investigate the pore network characteristics of three, common and widespread spring carbonate facies, as exposed in the Pleistocene Cakmak quarry (Denizli, Turkey): the extended Pond, the dipping crystalline Proximal Slope Facies and the draping Apron and Channel Facies deposits formed by encrustation of biological substrate. Integrating mercury injection capillary pressure, bulk and diffusion Nuclear Magnetic Resonance (NMR), NMR profiling and Brunauer–Emmett–Teller (BET) measurements with microscopy and micro-computer tomography (μ-CT), shows that NMR T_2 distributions systematically display a single group of micro-sized pore bodies, making up between 6 and 33% of the pore space (average NMR T_2 cut-off value: 62 ms). Micropore bodies are systematically located within cloudy crystal cores of granular and dendritic crystal textures in all facies. The investigated properties therefore do not reveal differences in micropore size or shape with respect to more or less biology-associated facies. The pore network of the travertine facies is distinctive in terms of (i) the percentage of microporosity, (ii) the connectivity of micropores with meso- to macropores, and (ii) the degree of heterogeneity at micro- and macroscale. Results show that an approach involving different NMR experiments provided the most complete view on the 3-D pore network especially when microporosity and connectivity are of interest.

1. Introduction

This study investigates the combined use of techniques for the understanding and quantification of 3-D pore network properties at different, linked scales in spring carbonates. These settings and their deposits gained renewed interest as valuable continental archives of environmental changes and as certain facies and fabrics are comparable to those found in potential subsurface carbonate reservoirs [*Kano et al.*, 2003; *Brasier et al.*, 2010; *Wright*, 2012; *Sharp et al.*, 2013; *Della Porta*, 2015; *Ronchi and Cruciani*, 2015].

Continental (hot) spring carbonates form where waters rich in Ca^{2+} and carbonate components emerge at the surface, cool down and degas while flowing downstream [*Brasier*, 2011; *Capezzuoli et al.*, 2014]. Spring systems therefore exhibit high rates of $CaCO_3$ precipitation across steep physical and chemical gradients along their outflow pathways [*Pentecost*, 2005; *Veysey et al.*, 2008]. In addition, changes in (microbial) biodiversity and metabolic activity systematically track these downstream gradients [*Fouke et al.*, 2003; *Zhang et al.*, 2004]. Several studies address in detail the wide range of depositional facies and fabrics typical of these environments [*Guo and Riding*, 1998; *Pentecost*, 2005; *Fouke*, 2011; *Okumura et al.*, 2012; *Gandin and Capezzuoli*, 2014; *Claes et al.*, 2015; *Della Porta*, 2015]. However, the petrophysical characteristics - and especially the presence, distribution and origin of microporosity - in these settings are less understood.

Spring carbonate deposits primarily form as a result of in-situ precipitation with a variety of primary, genetic pore types (framework, interlayer, fenestral, interpeloidal, . . .), and pore sizes [*Ahr et al.*, 2011; *Claes et al.*, 2015].

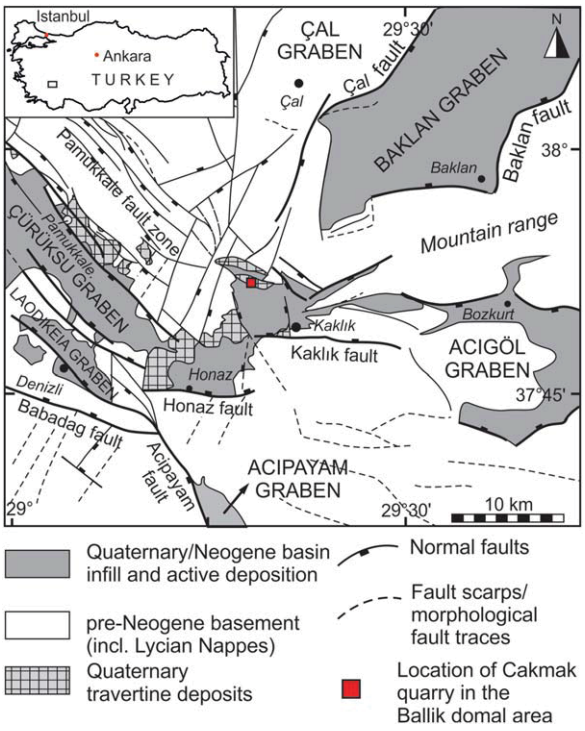

Figure 1. Location of the study area within the Denizli Basin (SW Turkey) (map modified after *Van Noten et al*. [2013]).

Travertine macroporosity, as visible in field photographs, has been quantitatively described by *Akin* [2009] to evaluate porosity changes due to weathering. *Soete et al*. [2015] report on V_p versus porosity paths that differ from those previously defined for marine carbonates. They found that acoustic velocity variations are linked to the dominant pore types present in different travertine deposits (macro- versus microporosity, cuboid versus rod shaped pores). Recently, *Ronchi and Cruciani* [2015] addressed for the first time the porosity and pore structure in subhorizontal tabular travertine bodies (Saturnia deposits, Italy) using Scanning Electron Microsopy (SEM), classical microsocopy, micro-computer tomography (μ-CT) and standard poroperm techniques. While they focus on pores above 25 μm diameter, they highlight the problem of heterogeneity in these deposits and suggest the importance of microporosity in addition to large, centimeter-sized pores.

Microporosity, if connected, could indeed drastically impact flow and solute transport [*Maliva et al*., 2009; *Volery et al*., 2010]. A recent study by *Chafetz* [2013] on hot spring carbonates describes shrubs, peloids and oncoids [*Chafetz and Folk*, 1984; *Chafetz and Guidry*, 2003; *Chafetz*, 2013], interpreting them as microbial fabrics and the enclosed microporosity as a result of microbial organic matter decay. The localized abundance of irregular shaped submicron- to micron sized pores in experimental precipitates with bacterial strains similarly let *Bosak et al*. [2004] suggest that microporosity could be a biomarker for the former presence of microorganisms and microbial involvement in carbonate precipitation. In summary, the presence of micropores in spring carbonate deposits seems ubiquitous, though remain poorly characterized. Better insights on size, shape and distribution of microporosity in travertine facies can contribute to our understanding of possible origins and potential impact on flow properties.

This study therefore aims (1) to investigate and quantify microporosity and its contribution within distinctive travertine facies based on (high-resolution) microscopy, pore size measurements and bulk NMR (Nuclear Magnetic Resonance), and (2) to evaluate pore connectivity and heterogeneity at different scales combining NMR profiling, NMR diffusion experiments and micro-computer tomographic (μ-CT) imaging. Testing the combination of advanced petrophysical and imaging methods helps the development of an approach to characterize the porous network in different continental spring carbonate facies. A number of core and plug samples are selected, originating from a large Pleistocene carbonate terraced spring system exposed in the Cakmak quarry of the Ballık area. The deposits are part of the well-known spring carbonate province in the Denizli Extensional Basin (Turkey) [*Özkul et al*., 2013] (Figure 1). Comparable deposits were studied, from a geobody perspective, in adjacent quarries by *Claes et al*. [2015]. The travertine deposits are composed of >94% calcite [*Özkul et al*., 2013]. Active springs at Pamukkale are of the Ca-Mg-SO_4-HCO_3-type. They emerge at temperatures of 35 to 57°C (pH: 6.0 to 7.4) and evolve downstream to temperatures of 20°C [*Pentecost et al*., 1997; *Kele et al*., 2011; *Özkul et al*., 2013]. Travertine carbon and oxygen isotopic values from the Ballık area [*Kele et al*., 2011; *Claes et al*., 2015] differ slightly from those of the recent travertine. This has been interpreted as a primary difference that reflects changes in spring fluid sources spatially or through time [*Özkul et al*., 2013]. Calculations of temperatures of deposition from $\delta^{18}O$ values of ancient travertine suggest average temperatures between 26 and 35°C [*Claes et al*., 2015] or 23 and 39° [*Özkul et al*., 2013]. The samples that are subject of this study reflect three common spring environments and depositional facies in the Ballık Pleistocene travertine; namely; the draping Apron and Channel, extended Pond and crystalline Proximal Slope Facies (Figure 2).

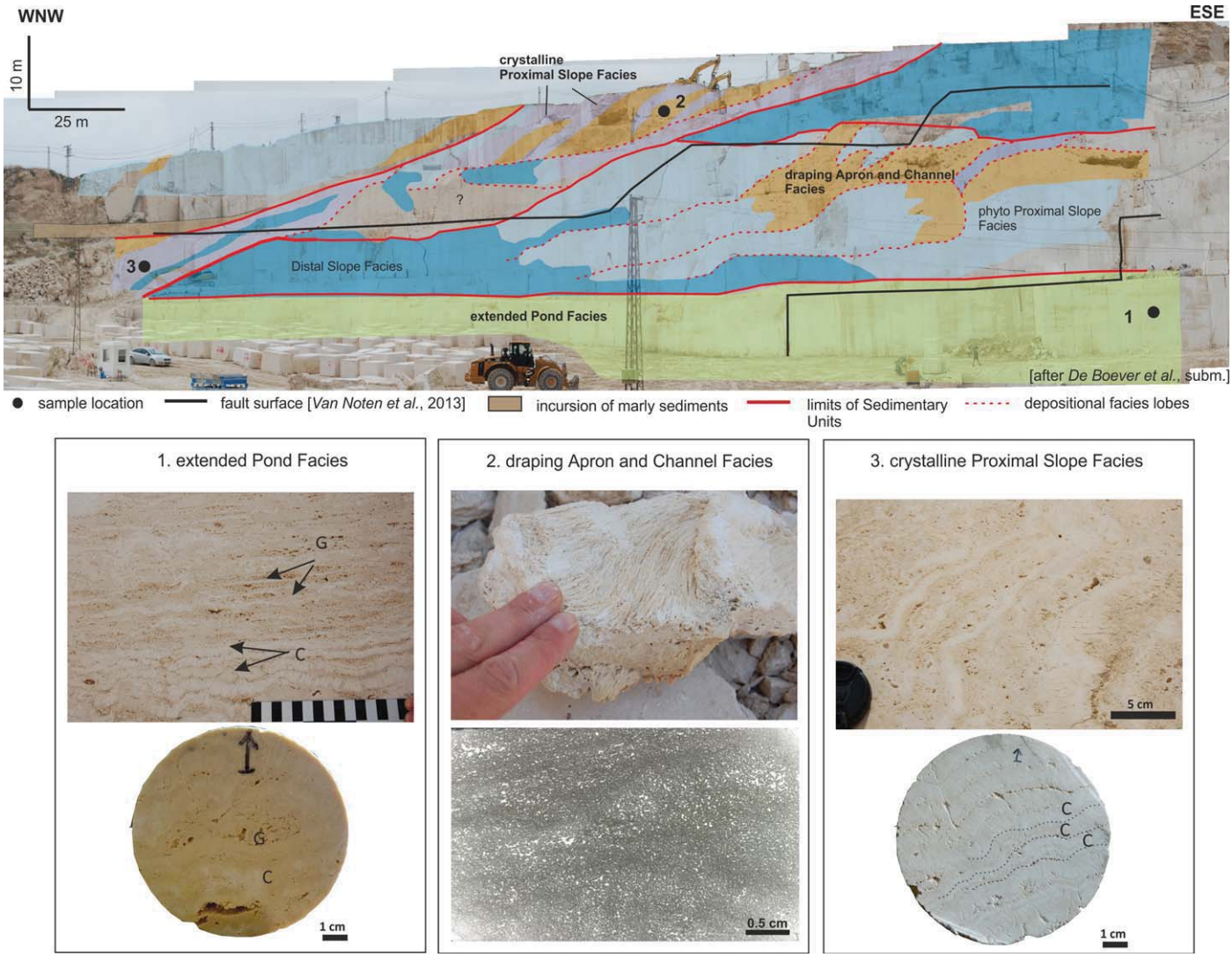

Figure 2. Overview of the depositional facies and sampling locations in the central-western part of the Cakmak quarry exposure (modified after [*De Boever et al*., subm.]). The three facies and key fabrics that are focus of this study are illustrated below. (left) Alternating granular and crust laminae in extended Pond Facies. Lower image is a frontal image of a core. (middle) Filamentous streamers form bundles that are finely laminated in thin section. (right) Predominance of the whitish, dendritic crust fabric in dipping laminae of the crystalline Proximal Slope Facies. G = granular fabric, C = crust fabric.

In this study, the term microporosity refers to pore sizes with diameters $\leq$ 1.0 μm, which is a common, reference spatial dimension with respect to flow in reservoir rocks and the size of microbial cells [*Madigan et al*., 2012]. *Hassall et al*. [2004] define mesopores as pores with diameters up to 5.0 μm and macropores with sizes above and these cut-off values are applied here.

2. Sample Material

The travertine deposits in the Cakmak quarry are exposed along a roughly WNW-ESE-oriented vertical wall. They reveal a single, smooth slope to terraced spring system, stepping down to the west-northwestern corner. A depositional model with detailed facies and fabric descriptions is presented by *De Boever et al*. [subm.] and illustrated in Figure 2.

Sample material for this study comes from three of the facies observed in the Cakmak quarry, namely; the extended Pond, the draping Apron and Channel Facies and the crystalline Proximal Slope Facies (Figure 2). These three facies do not represent the full suite of 5 depositional facies recognized in the quarry, but they are common in the studied outcrop, and are widespread and characteristic of other modern and ancient

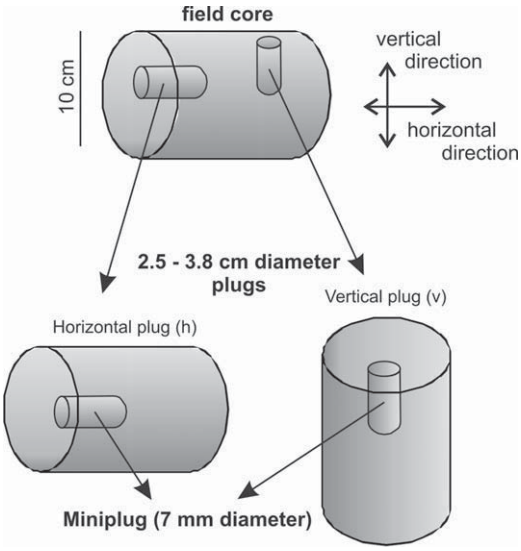

Figure 3. Orientation of cores and plugs.

travertine deposits around the world [*Guo and Riding*, 1998; *Chafetz and Guidry*, 2003; *Pentecost*, 2005; *Fouke*, 2011; *Gandin and Capezzuoli*, 2014; *Della Porta*, 2015].

The extended Pond Facies can be traced over a distance of tens of meters and is exposed at the bottom of the currently excavated quarry levels (Figure 2). Granular and crust macrofabrics alternate in very thin to medium sized, subhorizontal to undulating beds. The granular macrofabric consists of 0.1–1.5 mm diameter granules that form irregular, very thin laminae and up to 1 decimeter thick beds [*Guo and Riding*, 1998. The granular fabric consists of micritic to equant calcite crystals with dark, microporous crystal cores. They form amalgamated calcite crystal clusters with an irregular outline, or they build compact, radial dendritic structures. The crust macrofabric is composed of stacked layers of white, elongated (dendritic) crystals (Figure 2). The Apron and Channel Facies in the Cakmak deposits consists of filamentous streamer deposits that form decimetre-sized bundles. They result from the encrustation of a biological substrate, probably grasses [*Claes et al*., 2015]. They typically occur as features that hang down over and cover the crest of the Proximal Slope deposits. The crystalline Proximal Slope Facies is mostly composed of dense, low to strongly inclined dendritic crusts (Figure 2). They build smooth to terraced slopes of up to 10 meters high. Granular laminae occur as well, but are of less importance.

Three respresentative core samples were taken from the vertical quarry walls with a Stihl Model MS261 hand-held drill and a steel carbide core bit (10 cm diameter in width by 15–30 cm in length), in addition to two hand samples. The cores were further plugged two times vertically and two times horizontally in the lab as illustrated in Figure 3. Table 1 gives an overview of the selected sample set.

3. Methods

3.1. Microscopy

Conventional transmitted light and fluorescence microscopy of thin sections, using a Leica DM LP optical microscope, allowed examining the microscopic fabric (microfabric) and pore space in 2-D, at a micrometer resolution. Thin sections were impregnated with a resin, stained with a fluorescent dye (emitting at ca. 550 nm when excited at ca. 365 nm) to facilitate porosity observations. A scanning electron microscope

Table 1. Petrographical and Petrophysical Characteristics of the Studied Material[a]

Facies	Fabrics	Pore Type	Sample	Φ (%)	K_g (mD)	NMR Φ(%)	BET Surface (Kr, m^2/g)
Extended Pond	Granular and crust	Intra- and intercrystalline, framework	plug h	9.8; 12.1	112; 184	7.17	
			plug v	11.8; 13.8	743; 493	5.15	0.0629
Crystalline Proximal Slope	Crust (and granular)	Intra- and intercrystalline, framework	plug h	12.0; 12.5	295; 207	29.11	
			plug v	14.7; 14.6	249; 76.9	11.05	0.0300
Draping Apron-Channel	Streamer	Intraparticular, framework	plug h	13.5	28.5	1.83	
			plug v	15.2	298	30.51 (vug)	0.0895
			hand sample	21.3; 19.7	499; 1295		

[a]NMR-derived porosity estimates are based on the Halbach measurements. H= horizontal, v= vertical plug. For two plugs of field cores from the draping Apron and Channel Facies no porosity and permeability value could be obtained due to the presence of vugs at the side of the plug. Two additional measurements were therefore conducted on vertical plugs from two hand sample.

(SEM) FEI XL30 Sirion FEG, equipped with secondary electron (SE), backscatter electron (BSE) and energy dispersive detectors is used for higher-resolution observations of (micro)porosity.

3.2. Porosity (Φ), Permeability (K) and Mercury Injection Capillary Pressure (MICP) Measurements

Helium porosity and specific gas permeability measurements were carried out at PANterra Geoconsultants (the Netherlands) on cleaned and dried, 1 or 1.5 inch (2.5 or 3.8 cm) diameter plugs (Figure 3).

Mercury injection capillary pressure (MICP) experiments with an Autopure IV instrument (Micromeritics) are used to obtain a measure of the pore (throat) size distribution and are compared to pore size distributions obtained by NMR.

3.3. Nuclear Magnetic Resonance (NMR)

Two miniplugs (7 mm diameter) of each sample, one horizontal and one vertical (Figure 3), were used for NMR measurements. The miniplugs were saturated with de-ionized water for 12 h and sealed with water resistant parafilm prior to analysis.

3.3.1. Approach

Stray-field NMR can be employed to non-destructively characterize pore size distributions of porous materials [*Zinszner and Pellerin*, 2007]. NMR relies on the magnetic properties of atomic nuclei in NMR active isotopes such as ^{1}H in water. Atomic nuclei can be assimilated to magnetic dipoles that precess around a certain axis. For an extensive outline of the principles of NMR we here refer to *Casanova et al.* [2011] and *Zinszner and Pellerin* [2007].

The signal decay of transverse magnetization of a multi component material with *i* numbers of components can be ascribed as a sum of exponentials (equation (1)) [*Casanova et al.*, 2011]:

$$M(t) = \sum_{1}^{i} A_{0i} \exp\left(-t/T_{2i}\right) \tag{1}$$

with: A_{0i}: number of spins with a characteristic relaxation time T_{2i} (ms).

Such signal decays can be converted to distributions of relaxation times by an inverse Laplace transformation. The area under the curve between two specific relaxation time values is an estimate of the proportion of pore space with respect to those relaxation times [*Casanova et al.*, 2011]:

$$1/T_{2i} = 1/T_{2B} + \rho_2 * S/V + (1/12)\,(t_E * \gamma * G)^2 * D \tag{2}$$

With: T_{2B}: bulk relaxation time of the saturated fluid (ms); ρ_2: surface relaxivity (μm/s); S: specific surface of pore (m^2); *V*: pore volume (m^3); D: molecular self-diffusion coefficient; γ: gyromagnetic ratio of the investigated nucleus; G: magnetic field gradient; t_E: echo time of the CPMG sequence (Carr-Purcell-Meiboom-Gill) [*Carr and Purcell*, 1954; *Meiboom and Gill*, 1958].

When assuming that the average surface relaxivity per pore is nearly constant, the relaxation distribution corresponds to a distribution curve of the parameter V/S, reflecting a shape factor and pore surface rugosity. In water-saturated rocks, T_2 distributions are thus qualitatively related to pore-size distributions. The interpretations assume that only a very small quantity of ferrous/paramagnetic ions are present and that they are homogeneously distributed among the pore surfaces.

The calculation of the NMR pore size distribution assumes that molecules coming into contact with the pore surface by diffusion in one compartment are not mixed with molecules of other compartments or do not diffuse themselves to other compartments [*Fleury et al.*, 2007; *Fleury and Soualem*, 2009]. This effect is known as diffusional pore coupling and the overall effect is a shifting and merging of T_2 modes. It provides however a way to qualitatively describe the degree of connectivity or coupling between small (micro) and large (macro) pores.

The molecular self-diffusion can also be studied with stray-field NMR sensors such as the NMR-MOUSE®, profiting from their static magnetic field gradient, which is present in the sensitive volume [*Rata et al.*, 2006]. With a pulse sequence called stimulated-echo sequence, the molecular self-diffusion coefficient of water can be probed. For bulk water at 20°C, it has a value of $2.03 \times 10^{-9} m^2 s^{-1}$ and is reduced for water as present in porous systems due to restriction of the diffusion pathways by the pore walls. The sequence is divided into two parts, the encoding/mixing period, where three 90° pulses define two time sets δ and Δ,

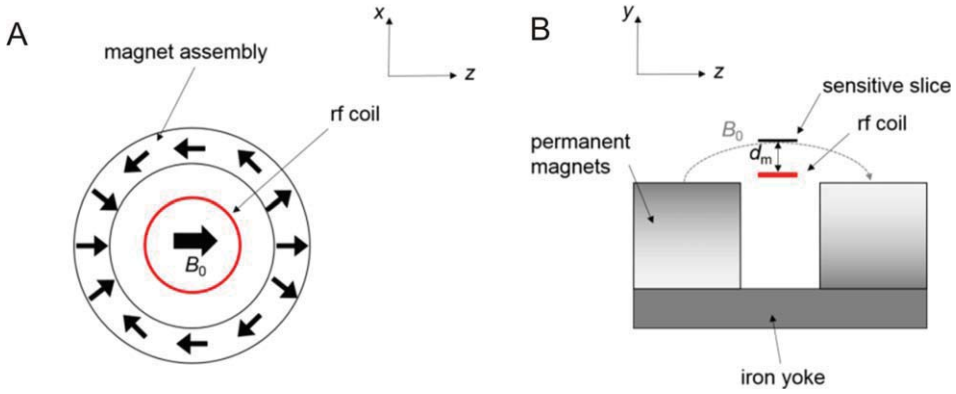

Figure 4. (a) Principle of the Halbach magnet design according to *Casanova et al.* [2011]. The sample is measured inside the magnet system. (b) Principle of the NMR-MOUSE® according to *Blümich et al.* [1998] and *Casanova et al.* [2011]. The signal is detected from a position outside the magnet assembly.

whit δ the encoding time that is incremented during the experiment, followed by a CPMG detection period. The self-diffusion coefficient is calculated from the slope of a linear fit of equation (3):

$$\ln\left(s(\delta)/s(0)\right) = -\gamma^2 G^2 \delta^2 \left(\Delta + {}^2/_3 \delta\right) D - {}^{2\delta}/_{T_2} - {}^{\Delta}/_{T_2} \quad (3)$$

With: γ: gyromagnetic ratio of the investigated nucleus; G: magnetic field gradient, D: molecular self-diffusion coefficient. The parameters are chosen in such a way that δ is $\ll T_2$ and Δ is $\ll T_1$, allowing to neglect the two last terms of equation (3).

3.3.3. Instruments

The NMR measurements were conducted on two different low-field NMR sensors at the Institut für Technische und Makromolekulare Chemie - RWTH Aachen (Germany) that can be distinguished by their general magnet design [*Halbach*, 1980; *Blümich et al.*, 1998, 2014; *Casanova et al.*, 2011] (Figure 4).

A Halbach magnet for cylindrical samples was used for relaxation experiments at 21MHz. The probe was operated with a Maran Ultra Spectrometer (Oxford Instruments). The radiofrequency (rf) coil is positioned in the center of the magnet and the magnetic field points into the *y*-direction This design leads to high homogeneity within the sensitive volume, which reduces the magnetic field gradient significantly, so that it can be neglected in equation (2).

The second sensor is a single-sided Profile NMR-MOUSE® [*Blümich et al.*, 1998] operated at 17 MHz with a KEA spectrometer (Magritek). It is employed for relaxation, diffusion and profile experiments. The NMR-MOUSE® is an open system and detects the NMR signal from a sensitive slice located in a certain distance to the magnet and coil surface (Figure 4b). The sensitive volume can be shifted non-destructively through the sample with a motor lift and NMR signals can be measured at different positions within the sample volume. The supporting information provides details on the comparison of the Halbach and Mouse measurements.

3.4. Kr-BET

Specific surface areas were determined from krypton gas adsorption at 77.3K (liquid N_2 bath), by means of the static-volumetric method, using a Quantachrome Autosorb-1 device equipped with an extra, low range (0–1.3 Pa) pressure transducer. The measurements were done on miniplug samples (mass: 1.5–5 g). One miniplug for each facies was measured and identical material was used as for NMR measurements to avoid heterogeneity effects when integrating the results. The miniplugs were dried and outgassed under vacuum at 130°C, until the pressure increase in the cell was less than 1.3 Pa/min. Adsorption was measured at 17 relative pressure steps between 0.01 and 0.4. A krypton saturation pressure (P0) of 0.351 KPa was used for each relative pressure point. Sorbate-sorbent equilibrium was assumed when the relative pressure was constant for 4 min at a tolerance of 0.012. The multipoint BET-method was applied to deduce the isotherm data. The relative pressure range for the BET regression was determined from Rouqeurol-plots [*Rouquerol et al.*, 2013]. A cross-sectional area for the krypton molecule of 0.205 nm^2 was used. Repeated

measurements on standard materials demonstrated that the accuracy and precision of the method is better than 2% (2 stdev.)

The krypton BET specific surfaces were used to approximate the NMR surface relaxivity ρ_2 according to equation (4), using the Halbach measurements [*Hossain et al*., 2011; *Vincent et al*., 2011]:

$$ {}^{1}/_{T_{2mS}} \cong \rho_2 * {}^{S_T}/_{V_T} \quad (4) $$

With: T_{2mS}: average relaxation time of the T_2 distribution (ms); S_T: total pore surface as determined by BET (m^2) and assuming that the surface explored by NMR and BET is the same; V_T: total pore volume (m^3), determined based on the miniplug weight, sample density and the plug porosity.

Obtaining an approximation for the surface relaxivity then permits to translate the T_2 modal distributions into volume to surface (V/S) ratios of compartments of the porous media, which is a measure of pore body diameter sizes.

3.5. 3-D Imaging With Micro-Computerized Tomography

3.5.1. μ-CT Setup and Image Reconstruction

3-D imaging with computerized tomography focused on miniplugs (diameter of 7mm). Projections are acquired using a Nanotom high-resolution X-ray μ-CT system from PHOENIX X-Ray (rotation: 360° in 0.2° steps). Samples were scanned at 4 μm resolution for full plug width images (80 kV tube voltage, 200 μA current) and at 2 μm pixel resolution for a Region of Interest (ROI) scan (90 kV tube voltage, 170 μA current). The Hamamatsu flat detector is made up of a 2300 × 2300 pixels grid. Averaging was set at 3 and detector shifting was allowed to reduce possible ring artefacts. Reconstruction of volumetric data uses a cone beam Feldkamp algorithm. The beam hardening effect is reduced by inserting a 0.1 mm Cu-filter during acquisition and a mathematical correction during the reconstruction process.

3.5.2. Image Analysis Workflow and Representative Elementary Volume (REV)

The image analysis workflow consists of (1) visualizing, segmenting (dual thresholding) and quantifying the resolved pore space (total porosity), (2) calculating the Representative Elementary Volume (REV) for porosity, and (3) labeling and visualizing all individual, separate pore volumes [*De Boever et al*., 2012]. Image treatment is carried out, using the Avizo Fire software package (Version 7.0, VSG, France) and Matlab.

The segmented, binary image slices of each scan are used to calculate the REV for porosity using a geostatistical approach. The REV allows evaluating whether porosity quantifications are representative for the volume and plug scale studied. It invokes the calculation of the semivariogram for the parameter porosity in multiple directions. The semivariogram sill value represents the plateau value of porosity attained. The range or length of correlation is the distance at which the sill value is reached in that direction. Semivariograms along multiple directions are combined to create a 3-D semivariogram surface that shows porosity heterogeneity and directions of porosity REV minima and maxima.

4. Results

4.1. Microscopic Fabric and Porosity

The well-laminated, extended Pond Facies (Figure 2) is characterized by stacked laminae of granular and crust fabrics. The granular fabric is composed of clustered micritic to equant calcite crystals with turbid crystal cores. Porosity between these crystal clusters can be classified as intercrystalline porosity (in the sense of *Choquette and Pray* [1970]) and has diameters above 20 μm (Figure 5a). SEM reveals additional intracrystalline porosity within the turbid crystal cores. This porosity is distributed randomly or aligned parallel to the crystal outline (Figure 5b). Similar inter- and intracrystalline porosity types occur between and within the feather crystals that build dendritic crusts (Figures 5c–5e). Intracrystalline porosity in dendritic structures can furthermore show fine alignments that can be traced over different crystals and remind of "growth bands" perpendicular to the crystal length axis (Figure 5d). Dendritic crusts that are prevalent in the crystalline Proximal Slope Facies have a comparable macro- and microfabric, but the crusts are denser, granular fabrics are less common and feather crystals might be asymmetric and curved.

The draping Apron and Channel Facies at Cakmak is mostly composed of the streamer fabric (in the sense of *Fouke* [2011]). The streamers consist of hollow tubes, 50–75 μm in diameter, with a micritic rim,

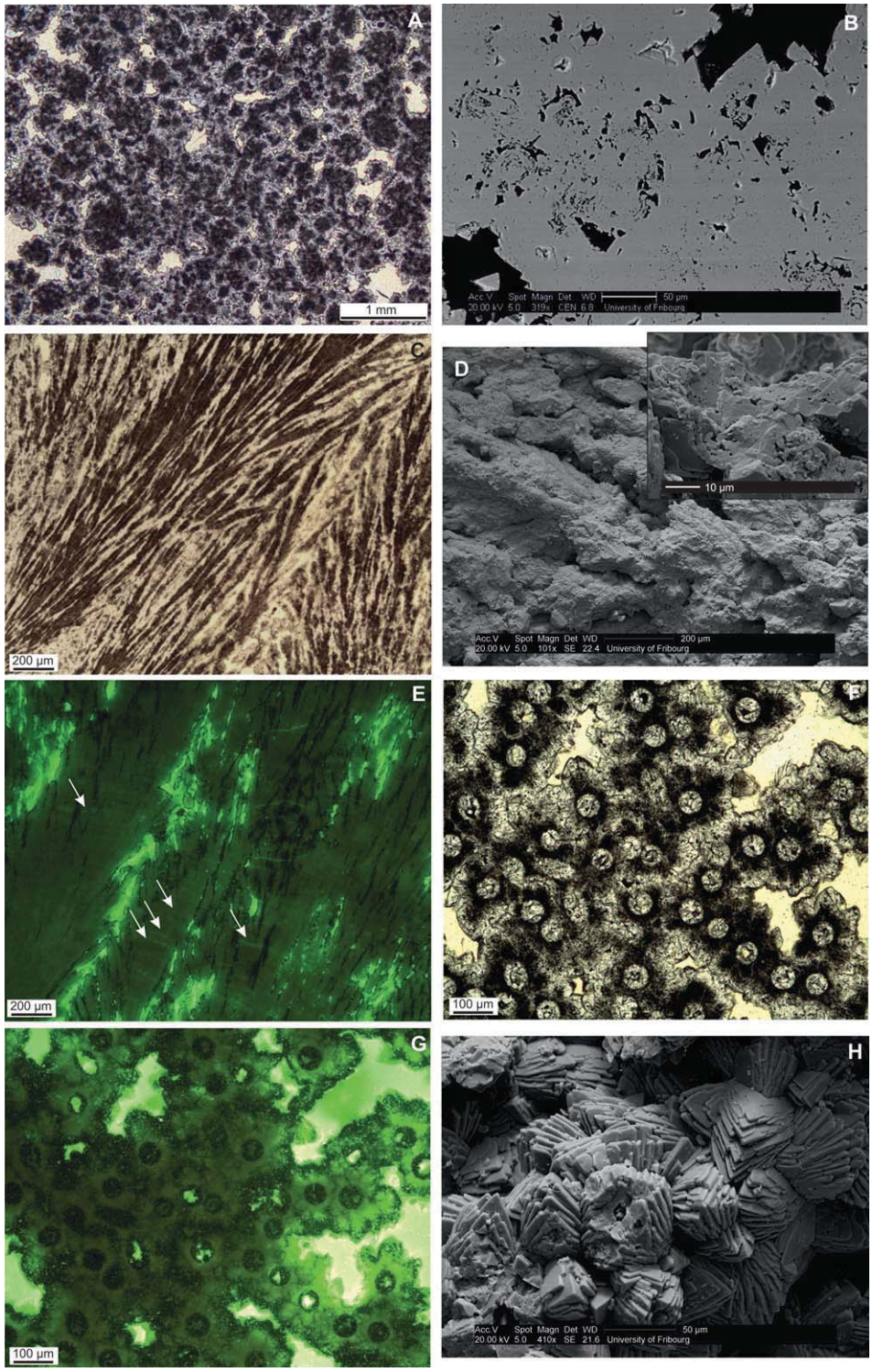

Figure 5. Microscopy of the studied fabrics. (a) Transmitted light image of a granular fabric in an extended Pond Facies sample. (b) BSE image of a granular fabric showing intra- and intercrystalline porosity. (c) Dendritic carbonate crystals in a crust fabric. The turbid crystal cores are surrounded by circumgranular, transparent calcite. (d) SE image of dendritic crystals in a crust fabric. Inset shows the intracrystalline porosity in the crystal cores. (e) Fluorescence image of a thin section, impregnated with a green fluorescing epoxy to highlight the porosity distribution. Within the dendrite crystals, fine laminae of variable intra-crystalline porosity are visible (white arrows). (f) Overview image of the streamer fabric along a section perpendicular to the streamer's length axes (transmitted light). (g) Same images as Figure 5f under fluorescent light with a green fluorescing epoxy that highlights the intercrystalline porosity and suggests intracrystalline porosity in the turbid crystal centres. (h) SE image of the rhombic $CaCO_3$ crystals that surround the intraparticular porosity of the streamers.

surrounded by compact, equant to very short dendrites (Figures 5f and 5g). Framework porosity between streamer "strings" and "intra-string" porosity (intraparticular (in the sense of *Choquette and Pray* [1970])) is incompletely filled with transparent calcite crystals. SEM reveals fine, intracrystalline porosity within the turbid, crystal cores (Figures 5b and 5h).

All facies furthermore display large intercrystalline porosity (Figures 5a and 5f) that results from the growth and packing of granular, dendritic or streamer components and as such can be refered to as "growth framework" porosity. Partly cemented, vuggy porosity is more rare, but was observed in one draping Apron and Channel Facies sample.

4.2. 3-D meso- to Macroporosity Characterization

Reconstructed pore volumes, based on μ-CT, allow visualizing the 3-D porosity distribution and comparing pore shapes in different rock samples. The maximum resolution is 2μm and implies that all porosity visualized concerns meso- to macropores.

Following pore segmentation, the total porosity in the studied 3-D volume is determined. In agreement with He-porosity values, the highest porosity percentages were encountered in the draping Apron and Channel Facies samples. However, the μ-CT-based quantifications systematically underestimate He-porosity values, suggesting an important part of the pores have sizes below the 2 to 4 μm^3 voxel resolution. This difference is highest for the extended Pond Facies samples.

The porosity REV for each of the samples is given in Table 2. The 3-D image volumes used in the calculations all exceed the sample REV at the respective resolution. At 4 μm resolution, the studied volume encloses different laminae. ROI scans at 2 μm resolution encompass one, single or two laminae. The REV is similar to slightly larger for 4 μm scans, compared to the scans at a resolution of 2 μm. The semivariogram ranges along the principal axes, x, y and z, differ (Table 2). It indicates that meso- to macroporosity is heterogeneously distributed for all samples.

The sample heterogeneity becomes even clearer when visualizing the 3-D surface of the variogram range (Figures 6a, 6c, and 6e). The orientation of the REV-limiting direction can be compared with 3-D images of the labeled pore space (Figures 6b, 6d, and 6f). The pronounced heterogeneity in draping Apron and Channel Facies samples is controlled by the aligned, interparticular streamer porosity (Figures 6a and 6b). The longest axis of the REV ellipsoids for extended Pond and crystalline Proximal Slope Facies samples lay approximately within or close to the plane of stratification, at high angle with the alternation of granular and/or crust laminae (Figures 6c–6f).

The labeled pore space, in which each individual pore body receives a separate colour (Figures 6b, 6d, and 6f) also provides a fast way to evaluate connectivity at the meso- to macroscale. In all samples the largest pore body makes up about 50% of the total pore space. 3-D visualization shows a preferential orientation and alignment of the pores in the draping Apron and Channel samples corresponding to the porosity between streamer bundles. This porosity is well-connected at the miniplug scale (Figure 6b). In

Table 2. μ-CT Data for Each of the Miniplugs and Scans[a]

	Resolution (μm)	Volume (mm^3)	Porosity %	REV r1 x (μm)	REV r1 y (μm)	REV r1 z (μm)
Pond h	4.00	208.74	6.50	182.4	218.0	155.6
	1.80	26.14	4.99	210.5	140.5	153.6
Pond v	4.00	208.98	10.37	217.9	225.3	241.3
	1.90	28.52	4.49	152.1	144.2	170.6
Proximal Slope h	4.00	210.13	11.70	127.4	74.8	72.4
	1.80	27.08	7.60	75.8	110.0	96.6
Proximal Slope v	4.00	311.54	14.80	70.4	62.3	113.2
	1.80	24.10	13.27	41.1	96.74	79.1
Apron-Channel h	4.00	206.90	14.54	197.5	213.0	237.0
	2.03	38.63	14.94	183.0	208.6	253.5
Apron-Channel v	3.75	206.74	12.80	219.9	217.9	290.0
	2.00	36.43	15.14	209.1	158.8	194.4

[a]Volume refers to volume analyzed. REV = Representative Elementary Volume. r1: range 1of the semivariogram in direction x, y, z.

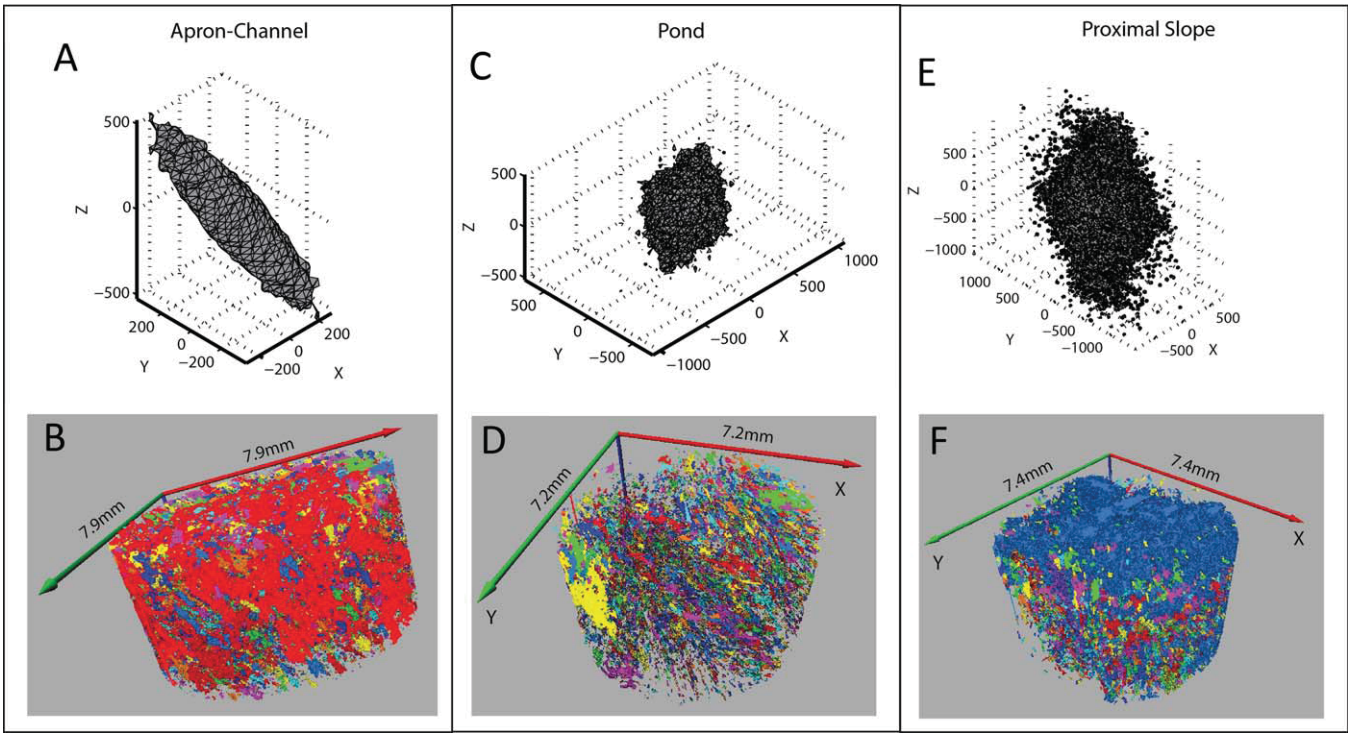

Figure 6. For each facies: 3-D porosity REV visualized by the surface of the semivariogram ranges and distribution of connected pore space. Each individual pore (not connected to others) is visualized by a separate colour. All scans at 4 μm resolution of 7 mm miniplugs, visualizing meso- and macropores. Height of the volumes shown, is 4 mm (z axis). (a, b) draping Apron and Channel Facies sample. Red pore is percolating. Porosity heterogeneity related to aligned streamer bundles is clearly visible. (c, d) Extended Pond Facies sample. REV length axis parallels the lamination. Yellow pore to the left is percolating, but numerous smaller, unconnected pores are present. (e, f) Crystalline Proximal Slope Facies sample. REV length axis parallels the lamination, at a high angle with the horizontal plane. The large blue-coloured pore space assures connectivity on the plug scale. It corresponds to intercrystalline porosity between feather crystals and framework porosity between dendrite bundles.

extended Pond and crystalline Proximal Slope Facies samples, connectivity between laminae is assured by pores between feather crystals, dendrite structures and larger, framework and vuggy pores. (Figures 6d and 6f).

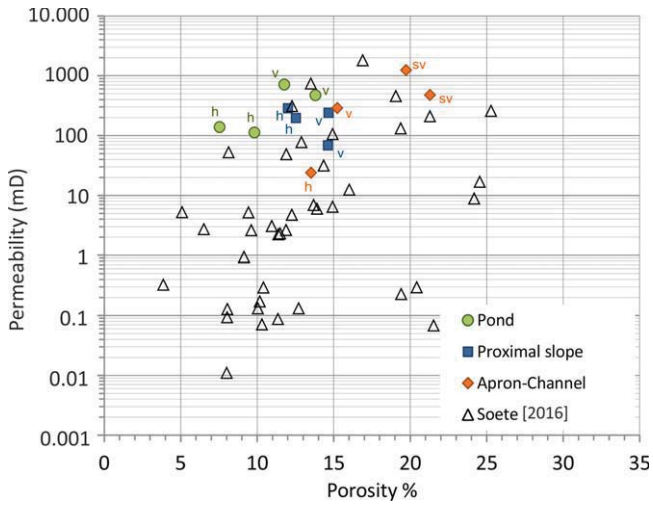

Figure 7. Porosity/permeability cross-plot for the Cakmak samples. H=horizontal plug, v= vertical plug, sv= hand sample vertical plug. White triangles: data after *Soete* [2016].

4.3. Pore Network From Petrophysical Measurements

4.3.1. Porosity-Permeability Properties

For each field core, two horizontal and vertical poroperm values were determined. As stratification is often at an angle with respect to the plug axes, no straightforward relation between horizontal/vertical permeability and laminae-orientation is apparent. Furthermore, the spread within a single facies is large (Figure 7). This is in agreement with previous findings [*Soete et al.*, 2015]. The draping Apron and Channel Facies samples seem to have the highest values, whereas the extended Pond Facies samples with granular and dendritic crust fabrics tend to have lower values (Figure 7 and Table 1).

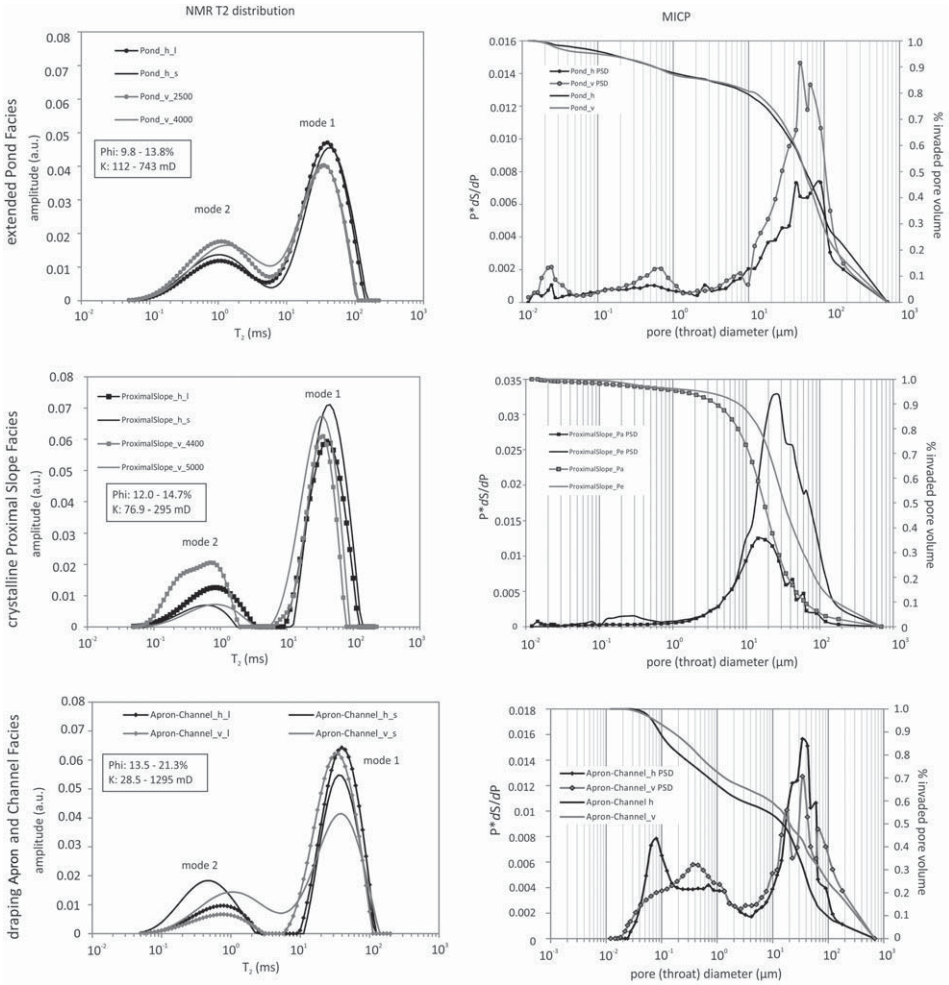

Figure 8. Petrophysical characteristics of miniplugs from the different Facies. h/v=horizontal/vertical miniplugs. l=miniplug lying on MOUSE® instrument, s=miniplug standing vertically up on MOUSE® instrument. PSD=Pore Size Distribution. a.u.=arbitrary unit.

The data indicate that a single porosity-permeability correlation for the travertine deposits can not be determined though roughly a positive correlation might be visible. This underlines the necessity to look into the actual 3-D pore network to understand the travertine petrophysical properties.

4.3.2. Pore Size Distributions

4.3.2.1. Extended Pond and Crystalline Proximal Slope Facies

Both the extended Pond and crystalline Proximal Slope Facies consist of a combination of granular and dendritic crust fabrics. The Pond samples show a bimodal NMR T_2 distribution with a main mode (1) between 35 and 40 ms and a subordinate mode (2) at 1 ms. It shows a poor bimodal pore throat size distribution, derived from MICP (Figure 8). The main MICP mode indicates pore (throat) sizes between 40 and 90 µm. A second and less prominent mode can be seen for pores with pore (throat) sizes of 0.5 to 0.7 µm in diameter. The Proximal Slope samples show a similar bimodal T_2 distribution. In comparison to the Pond samples, the main T_2 distribution mode 1 at 35 to 40 ms is much more dominant and communication with the secondary mode, with a maximum between 0.5 and 0.9 ms, is poor. The pore throat size distribution is unimodal to poorly bimodal. Again, mode 1 (15 to 25 µm) seems largely predominant over a very small mode 2 (around 0.3 µm) (Figure 8).

4.3.2.2. Draping Apron and Channel Facies

The streamer fabric shows consistent NMR and MICP responses (Figure 8). The NMR responses show a mode 1 at 31 to 39 ms and some variability in terms of the position of the smaller mode 2 (0.4 to 1 ms). Communication between mode 2 and mode 1 pore bodies is often poor, with exception of one of the vertical plugs. This plug contains vuggy porosity and possibly a dissolution phase ensured better pore body

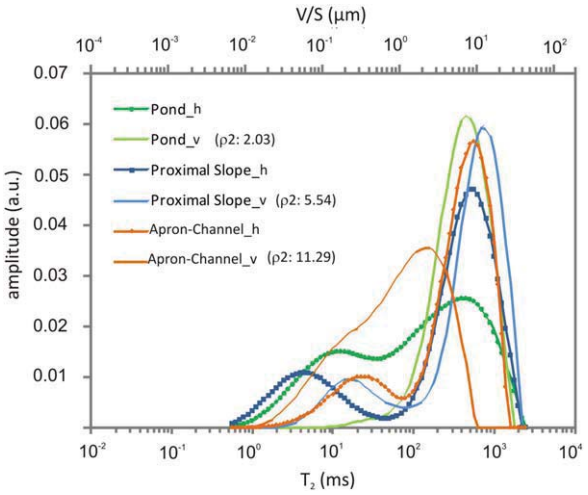

Figure 9. NMR T_2 distribution (Halbach) converted to V/S or "pore body diameter" distribution using BET specific surface area measurements to compute rho (ρ_2).

communication. The analyzed samples show a pronounced bimodal pore throat size distribution with a main mode 1 at 20 to 60 μm and a wide, smaller mode 2 with maxima for pore throat diameters between 0.07 and 1.7 μm.

4.3.3. Integration NMR and BET-Derived Specific Surface Area

In contrast to the MICP modal distributions, the dimensions of the pore media corresponding to the T_2 distribution modes in the NMR Halbach curves are not known. Based on independent BET measurements on the same miniplugs, Halbach responses can be converted into a distribution in terms of V/S (in μm) or pore body size (see equation (4)) and can be compared to MICP derived pore (throat) sizes (Figure 9). The results show that a pore body diameter of 1μm, the upper boundary of microporosity, corresponds to variable decay times, depending on the exact BET specific surface and the shape of the decay curve, namely; 57 ms for a crystalline Proximal Slope plug, 20 ms for a draping Apron and Channel Facies sample and 108 ms for the extended Pond Facies. This results in an average decay time of around 62 ms. It becomes also clear that, similarly to the MICP modal distributions, the subordinate, mode 2 in the NMR T_2 distributions can be linked to the presence of micropore bodies and the main mode 1 chiefly reflects macropores.

4.3.4. NMR Profiles and Self-Diffusion Experiments

Three miniplugs, one of each facies, were examined in more detail for their T_2 distribution along a depth profile using the NMR-MOUSE® (Figure 10). NMR profiling of watersaturated miniplugs can permit to gain more information on the sample heterogeneity in terms of (micro)pore structure.

The extended Pond Facies sample could be profiled over a total distance of 4 mm and shows a consistent bimodal distribution with changes in the relative importance of mode 1 (10–100 ms) versus mode 2 ($\leq$ 1 ms). These alternations occur over spatial distances of $<$0.5 and 1 mm. The crystalline Proximal Slope sample was only logged over 1 mm depth. The results show a very consistent bimodal distribution with a high, dominant mode 1 and a small mode 2, very consistent with the Halbach measurements. The streamer fabric of the draping Apron and Channel Facies sample was equally logged over 1 mm depth and shows a chiefly unimodal distribution and a gradual transition to a bimodal distribution at one end. It suggests that heterogeneity along the vertical miniplug axis is less pronounced and/or in the range of 1 mm or larger.

The self-diffusion coefficients of three miniplugs were studied with respect to the alignment of the miniplug to the *y*-direction of the magnetic field gradient (Figure 11). Therefore, each miniplug was measured in standing and lying position on the rf-coil, thus automatically probing anisotropy of self-diffusion. The molecular self-diffusion coefficients are a measure for molecular mobility, in this case, in the rock pore space. It is mainly influenced by Brownian motion and reflects effects such as surface relaxivity, pore size and shape. The miniplug from the crystalline Proximal Slope shows the highest self-diffusion coefficients, reflecting the relative importance of larger pore radii. The extended Pond sample has the highest anisotropy in self-diffusion, reflected in highly different values for the "standing" and "lying" diffusion experiment. The results of the draping Apron and Channel miniplugs do not document important anisotropy.

5. Discussion

The poro-perm characteristics of travertine deposits indicate the need to incorporate information on the pore size distribution, micro- to macropore connectivity and heterogeneity to describe the pore structure and eventually differentiate rock-types.

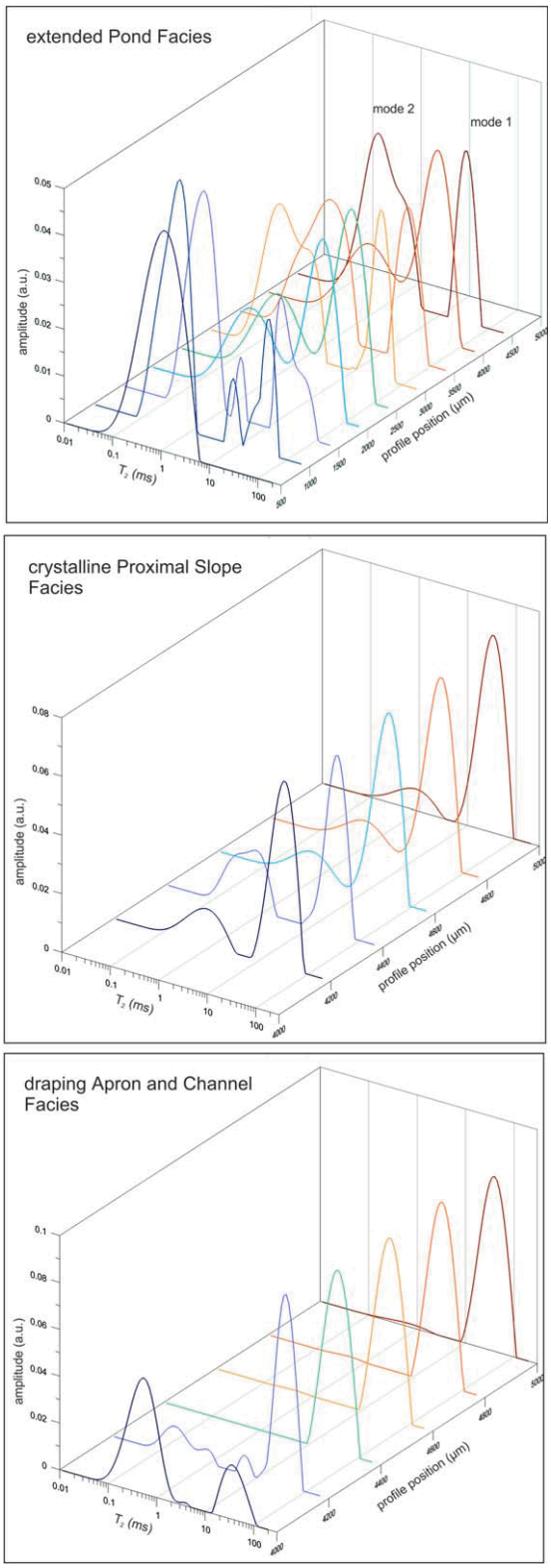

Figure 10. NMR-MOUSE® profiles at different heights of an extended Pond, crystalline Proximal Slope and draping Apron and Channel Facies miniplug showing heterogeneity in the NMR signal for the different samples (total height of 1–4mm).

5.1. Microporosity

The Halbach T_2 modal distributions have been translated into pore body size distributions using the BET-derived specific surface area. This allowed determining an average T_2 cut-off value for microporosity (1 µm) of 62 ms for the limited number of continental spring carbonate samples studied so far. *Vincent et al.* [2011] saw that within a set of marine carbonate reservoir rocks, microporous samples typically had a T_2 mode below 200 ms which corresponded, for their samples, to pore body diameters of 2 µm. Our results for continental spring carbonates thus show a slightly lower cut-off, but values are roughly in the same range.

Based on the T_2 cut-off values and the total area below the T_2 distribution curve for each sample, the relative contribution of microporosity to the total porosity can be quantified. Table 3 summarizes the results. Microporosity constitutes, in average, about 20% of the total porosity in the studied spring carbonate samples with variations between 6 and 33%. The results suggest a highly variable contribution of microporosity in the extended Pond Facies samples. This is in agreement with the strong heterogeneity seen in the NMR T_2 distribution along a depth profile of the miniplug and could relate to rapidly changing physico-chemical and possibly microbial-related precipitation processes through time or in micro-environments [*Jones and Peng*, 2012]. A slightly lower microporosity percentage is found for the crystalline Proximal Slope miniplugs and a consistent percentage, around 22%, in the draping Apron and Channel Facies miniplugs. In general, the values in the studied travertine samples are high and approach ranges that are typically described for chalks [*Maliva et al.*, 2009]. However, some caution is needed and the quantifications should be regarded as an approximation and as maximum values. Several of the T_2 modal distributions suggest communication between pore bodies of different sizes. This may result in diffusional pore coupling and shifts in the T_2 modes. Especially the larger T_2 mode 1 may be shifted toward shorter relaxation times [*Fleury et al.*, 2007; *Vincent et al.*, 2011]. The latter will affect (enlarge) the area below the T_2 curve for a certain microporosity cut-off T_2 value.

In terms of origin and distribution of the micro-sized pores, SEM observations demonstrate that they are mostly located within the core of calcite crystals in all facies studied. This intracrystalline

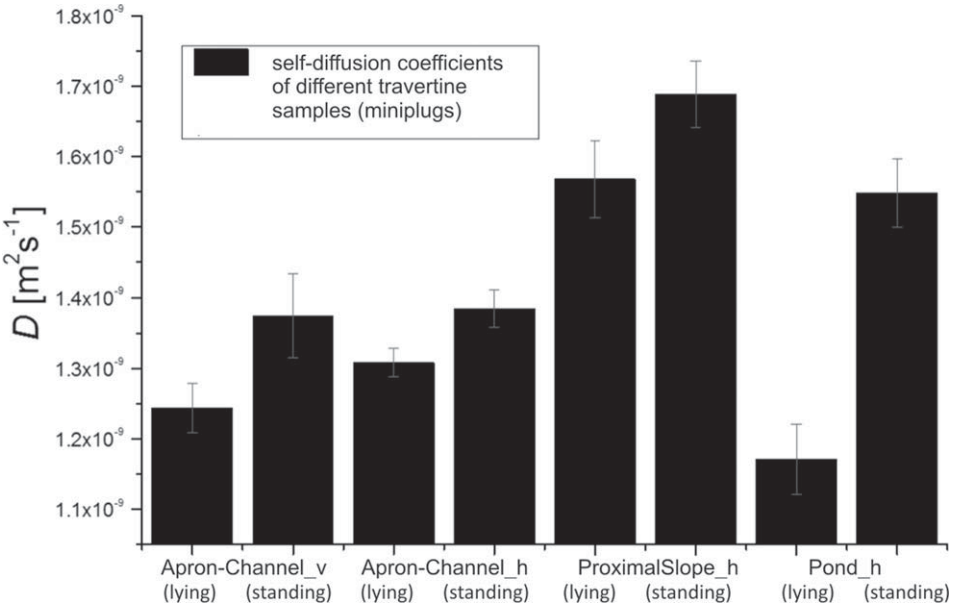

Figure 11. Molecular self-diffusion coefficients of water, measured with the NMR-MOUSE® on vertically (v) and horizontally (h) taken miniplugs.

microporosity is furthermore found systematically within the centre of grouped calcite crystals in the granular fabric, in the centre of feather crystals in dendritic crusts and in the short, dendritic structures that surround the streamer filaments giving them the typical turbid, dark appearance. The NMR and MICP modal distributions indicate the presence of only one group of micropores, in terms of size. The investigated petrographical and petrophysical results therefore do not show size or shape differences that differ for the distinct facies and do not provide a hint as to a potential origin of the micropores [see e.g., *Bosak and Newman*, 2005; *Bosak et al*., 2004; Folk and *Chafetz*, 2000].

5.2. Pore Connectivity and Heterogeneity

Descriptions of genetic pore types, based on 2-D petrography have been previously used in the case of marine carbonates as a start to re-group rocks into rock-types [*Westphal et al*., 2005; *Vincent et al*., 2011; *Brigaud et al*., 2014]. This approach does not fully work for the studied travertine rocks where intra-, intercrystalline and framework porosity are equally distributed in all three facies and fabrics.

It should be noted that a transparent calcite crystal rim precipitated around granular, streamer and dendritic textures in all facies (Figures 5a, 5c, and 5f). It hence modifies and reduces the size of intercrystalline porosity, but does not block pore connectivity, even not between intracrystalline microporosity and intercrystalline meso- to macropores. The exact timing of precipitation of this crystal rims is difficult to determine as early diagenetic phases in continental carbonates often result from the same or very similar fluids and precipitation takes place within the same depositional setting [*Pentecost*, 2005]. As such, these early precipitates are considered integral part of the primary spring carbonate fabric. Their isotopic signature also differs

Table 3. Approximation of Microporosity Contribution to the Total Porosity as Derived From the Area Under the T_2 Distribution Curve and a T_2-Equivalent Cut-Off Value of 1 μm[a]

Sample	Total Φ_{He}%	$T_{2\ mean}$ (ms)	S_T (m^2)	V_T (m^3)	ρ_2 (μm/s)	Φ_{micro}%	Φ_{macro}%
Extended Pond_v	11.8; 13.8	378.89	2.65 e-1	2.04 e-7	2.03	6.0	94.0
Extended Pond_h	9.8; 12.1	87.48			8.79	32.9	67.1
Crystalline Proximal Slope_v	14.7; 14.6	347.29	1.19 e-1	2.29 e-7	5.54	16.6	83.4
Crystalline Proximal Slope_h	12.0; 12.5	160.72			11.96	21.4	78.6
Draping Apron-Channel_v	15.2	57.74	3.56 e-1	2.32 e-7	11.30	20.8	79.2
Draping Apron-Channel_h	13.5	245.10			2.66	23.2	76.8

[a]S_T = total surface from Kr-BET measurements. V_T = total volume from water saturation measurements. ρ_2 = surface relaxivity.

from those of secondary cements along later fractures or in centimetre- to decimetre-sized voids [*El Desouky et al*., 2015].

The integration of NMR, MICP, BET and μ-CT carries the potential to qualitatively evaluate the micro to macro pore connectivity and heterogeneity in different facies. The extended Pond and crystalline Proximal Slope Facies are characterized by similar granular and crust fabrics, with the former fabric being more prominent in the extended Pond Facies. On the one hand, NMR bulk and profile T_2 distributions and NMR diffusion experiments systematically indicate the predominance of larger, meso- to macropore bodies in the crystalline Proximal Slope samples. These meso- to macropores seem poorly connected to any micropores present. On the other hand, microporosity is relatively more important in the extended Pond Facies samples and the connectivity between micro- and meso- to macroporosity is more consistent than observed for the crystalline Proximal Slope samples. T_2 modal distributions for the draping Apron and Channel Facies samples show that communication between micro- and meso- to macropores is variable.

At the meso- to macroscale, μ-CT images show that all facies possess well-connected pore networks. Intercrystalline pores between feather crystals and framework porosity between crust laminae assure connectivity parallel and perpendicular to the layering in the extended Pond and crystalline Proximal Slope plugs. In draping Apron and Channel Facies samples, a very well connected 3-D meso- to macroporosity network is controlled by aligned pore bodies between streamers and streamer bundles.

Differences are seen, in terms of heterogeneity, when microporosity is taken into account (NMR) or not (μ-CT). For an extended Pond Facies sample, the submillimetre-scale alternations observed in NMR profiles point, to small-scale layering within dendritic crust laminae. This can furthermore be observed using fluorescence microscopy, as shown in Figure 5e. This layering is finer and superposed on the alternation of granular and dendritic crust laminae at a scale of one to several millimetres (Figure 2). It points to the importance of multiscale heterogeneity, linked to layering in many travertine facies. This heterogeneity also results in the diffusion anisotropy in the extended Pond Facies sample. Higher values for the diffusion coefficient, D, were measured along a plane parallel to the fabric laminae (Pond_h; standing in Figure 11). In the lying position, diffusion is slower as micropores are dominant over meso- to macropores in the analyzed volume. When only intercrystalline and framework meso- to macropores are taken into account, such as in μ-CT data, the porosity heterogeneity is less obvious., Though it is still present as documented by the slightly ellipsoidal shape of the 3-D REV (Figure 6). In summary, preferential, layer parallel flow at field scale is most likely, but these plug-scale observations show that cross-layer flow is clearly not hindered.

The Apron and Channel Facies samples show a slightly different pattern with more prominent heterogeneity in the meso- and macroscale pore network based on μ-CT data (Figure 6), and no indications for a superposed, smaller scale heterogeneity in microporosity distribution. The diffusion experiment results show comparable molecular self-diffusion coefficients in different directions. The pore network is thus well connected both in a direction parallel to the streamers as in directions at high angles to that. At the outcrop, streamer bundles typically drape and fan out over the Proximal Slope deposits in different directions and form an open, porous framework in plugs.

The crystalline Proximal Slope Facies samples seem to represent a case in between, with little heterogeneity on the microporosity scale and somewhat higher heterogeneity at meso- to macroscale (3-D REV in Figure 6), compared to the extended Pond Facies. A single population of meso- to macroporosity is dominant in all measurements, but porosity values often do not reach as high as those for Apron and Channel Facies samples.

5.3. Toward Modeling and Permeability Estimates?

In addition to understanding the pore network and the role of microporosity, predictions of the flow properties of travertine rocks, based on NMR (wireline log) measurements, are of special interest in reservoir studies. In siliclastic rocks, two empirical permeability equations, based on NMR T_2 modal distributions, are widely used; the Schlumberger-Doll Research (SDR) equation and the Timur-Coates equation [*Freedman*, 2006]. They provide estimates of brine permeabilities (K_{SDR}) in water-saturated rocks. We here focus on the SDR equation as it uses the T_{2LM} (logarithmic mean of the T_2 distribution), which is a measured parameter that is directly influenced by the T_2 modal distribution and sensitive to small changes in this distribution [*Westphal et al*., 2005; *Brigaud et al*., 2014].

Table 4. Calculation of the SDR Parameter a_{SDR} Based on Air Permeability and NMR-Derived Porosity[a]

	$T_{2\ mean}$ (ms)	S_T (m^2)	V_T (m^3)	ρ_2 (μm/s)
Extended Pond	378.89	0.26	1.88 e-7	2.03
Crystalline Proximal Slope	347.29	0.12	2.30 e-7	5.54
Draping Apron-Channel	245.10	0.36	2.32 e-7	11.29

[a]Kg = air permeability (mD).

$$K_{SDR} = a * (\varnothing_{NMR}/100)^4 * T_{2LM}{}^2 \quad (5)$$

Where φ_{NMR} = total porosity as derived from T_{2i} (in percentage); T_{2LM}: logarithmic mean of the T_2 distribution (ms); a: empirical proportionality constant (m^2/ms^2)

From an extensive study of reservoir carbonates with a variety of porosity values, *Westphal et al*. [2005] proposed a set of values for the parameter a_{SDR} in function of the dominant pore type. For secondary, intercrystalline pores, a value for a_{SDR} of 1.59 is suggested. Carbonates dominated by vuggy porosity imply a parameter a_{SDR} of 0.0014, whereas for intra- and interparticle (primary) porosity, values of 0.04 and 0.55 are proposed respectively. Using the air permeability values of the samples and the total porosity, the parameter a can be approximated for the studied material (Table 4). Values range between 0.0001 and 0.3571. They are, in average, lower than those found by *Westphal et al*. [2005] for marine carbonates. The lowest values were found for the Proximal Slope samples where larger framework pore bodies are relatively more important (Figure 10). Where microporosity becomes more prevalent, the factor a_{SDR} increases.

Permeability estimates based on NMR distributions, using the above values for a in the SDR equation, should be seen as approximations due to (i) the bimodal pore size distributions and (ii) the variety of pore shapes in travertine samples. Overestimation is to be expected, for similar reasons as for the microporosity estimates. Diffusional pore coupling between micro- and meso- to macroporosity in some of the facies will affect T_{2LM} and as such k_{SDR}. The estimate is furthermore based on miniplug measurements. Heterogeneity on the centimetre- to decimetre-scale will affect permeability as well [*Ronchi and Cruciani*, 2015]. An appropriate upscaling approach is needed to incorporate NMR plug-based results into larger scale flow simulations.

6. Conclusions

This study presented the combined use of advanced imaging and petrophysical techniques (NMR-MICP-BET) to understand the 3-D pore network of continental spring carbonate deposits on a submicrometer to centimetre scale, with a special focus on microporosity. The suite of travertine samples from the Pleistocene Cakmak quarry (Turkey) reflect common and widespread facies and fabrics of carbonate spring deposits, the extended Pond Facies, the dense and dipping crystalline Proximal Slope Facies and the draping Apron and Channel Facies, formed by encrustation of a biological substrate. As such, the results could provide some basic and first insights in the pore structure, origin and connectivity in spring carbonate facies at other settings worldwide. Porosity and permeability values of the studied material range between 9.8 and 21.3% and 112 and 1295 mD respectively.

The results can be summarized as follows:

1. Based on BET and NMR measurements, an average T_2 cut-off value for microporosity of 62 ms (range: 24–110 ms) is proposed and microporosity percentages show a broad range between 6 and 33%. This range could be related to the presence or absence of (sub)millimetre scale heterogeneity and laminae within feather crystals that is detected in NMR measurements.
2. Microporosity is chiefly located within the cores of cloudy calcite in granular calcite crystal clusters and in feather crystals of dendritic structures in all facies. The investigated petrographical and petrophysical characteristics did not demonstrate differences in micropore size or shape for distinct facies.
3. All three facies show an uni- to bimodal MICP and bimodal NMR T_2 distribution with a microporosity mode (pore bodies below 1 μm diameter) and a meso- to macroporosity mode. The pore networks for the different facies are distinct in terms of (i) the relative importance of microporosity, showing a wide range and including the highest value in the extended Pond Facies samples, (ii) the connectivity of

microporosity with meso- to macropores being highest in the extended Pond Facies plugs and lowest in the crystalline Proximal Slope plugs, and (iii) the degree of heterogeneity, being most pronounced in the extended Pond Facies samples on a micro- to macroscale, and in the draping Apron and Channel Facies samples when only meso- to macropores are considered. The latter relate to the aligned streamer bundles that characterize this facies.

4. The results allow approximating values for parameter *a* in the SDR equation for permeability estimation based on NMR T_2 modal distributions. Values for a_{SDR} are in the order of 0.0001–0.3571.

To conclude, the results show that the combination of different NMR experiments in our approach provide the most complete view on the pore structure of the spring carbonate samples, in addition to classical poro-perm analyses. This is especially true when microporosity and millimeter-sized laminations are of particular interest.

Acknowledgments

Funding for this project is provided by TOTAL E&P (project FR5585). D. Oligschlaeger received separate funding through DFG (BL 231/42-1 and SCHN 587/9-1). Special thanks go to the quarry owners and managers of the Cakmak quarry (Turkey) for facilitating sampling. We appreciate support from B.W. Fouke (University of Illinois at Urbana-Champaign, USA) for discussions on travertine facies. G. Pyka is thanked for his help with the μ-CT measurements and H. Nijs is acknowledged for thin section preparation. The questions and detailed suggestions of two reviewers helped to further improve the manuscript. The data used are listed in the references, tables, figures and supporting information.

References

Ahr, W. M., E. A. Mancini, and W. C. Parcell (2011), Pore characteristics in microbial carbonate reservoirs, paper presented at AAPG Annual Conference and Exhibition, Houston, Tex.

Akin, M. (2009), Investigation of the macro pore geometry of yellow travertines using the shape parameter approach, *Environ. Eng. Geosci.*, *3*, 197–209.

Blümich, B., P. Blümler, G. Eidmann, A. Guthausen, R. Haken, and U. Schmitz (1998), The NMR-mouse: Construction, excitation, and applications, *Magn. Resonance Imaging*, *16*(5-6), 479–484.

Blümich, B., S. Haber-Pohlmeier, and W. Zia (2014), *Compact NMR, De Gruyter Textbook*, Berlin.

Bosak, T., and D. K. Newman (2005), Microbial kinetic controls on calcite morphology in supersaturated solutions, *J. Sediment. Res.*, *75*(2), 190–199, doi:10.2110/jsr.2005.015.

Bosak, T., V. Souza-Egipsy, F. a. Corsetti, and D. K. Newman (2004), Micrometer-scale porosity as a biosignature in carbonate crusts, *Geology*, *32*(9), 781, doi:10.1130/G20681.1.

Brasier, A. T. (2011), Searching for travertines, calcretes and speleothems in deep time: Processes, appearances, predictions and the impact of plants, *Earth Sci. Rev.*, *104*(4), 213–239, doi:10.1016/j.earscirev.2010.10.007.

Brasier, A. T., J. E. Andrews, A. D. Marca-Bell, and P. F. Dennis (2010), Depositional continuity of seasonally laminated tufas: Implications for δ18O based palaeotemperatures, *Global Planet. Change*, *71*(3-4), 160–167, doi:10.1016/j.gloplacha.2009.03.022.

Brigaud, B., B. Vincent, C. Durlet, J.-F. Deconinck, E. Jobard, N. Pickard, B. Yven, and P. Landrein (2014), Characterization and origin of permeability–porosity heterogeneity in shallow-marine carbonates: From core scale to 3D reservoir dimension (Middle Jurassic, Paris Basin, France), *Mar. Pet. Geol.*, *57*, 631–651, doi:10.1016/j.marpetgeo.2014.07.004.

Capezzuoli, E., A. Gandin, and M. Pedley (2014), Decoding tufa and travertine (fresh water carbonates) in the sedimentary record: The state of the art, *Sedimentology*, *61*(1), 1–21, doi:10.1111/sed.12075.

Carr, H. Y., and E. M. Purcell (1954), Effects of Diffusion on Free Precession in Nuclear Magnetic Resonance Experiments, *Phys. Rev.*, *94*, 630–638.

Casanova, F., J. Perlo, and B. Blümich (Eds.) (2011), *Single-Sided NMR*, Springer, Berlin.

Chafetz, H. S. (2013), Porosity in bacterially induced carbonates: Focus on micropores, *AAPG Bull.*, *97*(11), 2103–2111, doi:10.1306/04231312173.

Chafetz, H. S., and R. L. Folk (1984), Travertines: Depositional morphology and the bacterially constructed constituents, *J. Sediment. Petrol.*, *54*(1), 289–240.

Chafetz, H. S., and S. A. Guidry (2003), Deposition and diagenesis of Mammoth Hot Springs travertine, Yellowstone National Park, Wyoming, USA, *Can. J. Earth Sci.*, *40*, 1515–1529, doi:10.1139/E03-051.

Choquette, P. W., and L. C. Pray (1970), Geological nomenclature and classification of porosity in sedimentary carbonates, *Am. Assoc. Pet. Geol. Bull.*, *54*(2), 207–250.

Claes, H., J. Soete, K. Van Noten, M. M. El Desouky, H. Erthal, M. Vanahecke, F. Özkul, and R. Swennen (2015), Sedimentology, 3D geobody reconstruction and CO2-source delineation of travertine palaeo-deposits in the Ballık area., *Sedimentology*, *62*(5), 1408–1445, doi:10.1111/sed.12188.

De Boever, E., C. Varloteaux, F. H. Nader, a. Foubert, S. Békri, S. Youssef, and E. Rosenberg (2012), Quantification and prediction of the 3D pore network evolution in carbonate reservoir rocks, *Oil Gas Sci. Technol.*, *67*(1), 161–178, doi:10.2516/ogst/2011170.

De Boever, E., A. Foubert, B. Lopez, R. Swennen, C. Jaworowski, M. Özkul, A. Virgone, subm. Comparative study of the Pleistocene Cakmak Quarry (Denizli Basin, Turkey) and Modern Mammoth Hot Springs deposits (Yellowstone National Park, USA), Quaternary International.

Della Porta, G. (2015), Carbonate build-ups in lacustrine, hydrothermal and fluvial settings: Comparing depositinoal geometry, fabric types and geochemical signature, in Microbial Carbonates in Space and Time: Implications for Global Exploration and Porduction, edited by D. W. J. Bosence et al., *Geol. Soc. London Spec. Publ. 418*, 1–17, in press.

El Desouky, H., J. Soete, H. Claes, M. Özkul, F. Vanhaecke, and R. Swennen (2015), Novel applications of fluid inclusions and isotope geochemistry in unravelling the genesis of fossil travertine systems, *Sedimentology*, *62*, 27–56.

Fleury, M., and J. Soualem (2009), Quantitative analysis of diffusional pore coupling from T2-store-T2 NMR experiments., *J. Colloid Interface Sci.*, *336*(1), 250–259, doi:10.1016/j.jcis.2009.03.051.

Fleury, M., Y. Santerre, and B. Vincent (2007), Carbonate rock-typing from NMR relaxation measurements, *Proceedings of the SPWLA 48th Annual Logging Symposium*, 1–14.

Folk, R. L., and H. S. Chafetz (2000), Bacterially induced microscale and nanoscale carbonate precipitates, in *Microbial Sediments*, edited by R. E. Riding and S. M. Awramik, pp. 40–49, Springer, Berlin.

Fouke, B. W. (2011), Hot-spring Systems Geobiology: Abiotic and biotic influences on travertine formation at Mammoth Hot Springs, Yellowstone National Park, USA, *Sedimentology*, *58*(1), 170–219, doi:10.1111/j.1365-3091.2010.01209.x.

Fouke, B. W., G. T. Bonheyo, B. Sanzenbacher, and J. Frias-lopez (2003), Partitioning of bacterial communities between travertine depositional facies at Mammoth Hot Springs, Yellowstone National Park, USA, *Can. J. Earth Sci.*, *40*, 1531–1548, doi:10.1139/E03-067.

Freedman, R. (2006), Advances in NMR Logging, *Schlumberger Oilfield Services*, 60–66.
Gandin, A., and E. Capezzuoli (2014), Travertine: Distinctive depositional fabrics of carbonates from thermal spring systems, *Sedimentology*, *61*, 264–290.
Guo, L., and R. Riding (1998), Hot-spring travertine facies and sequences, Late Pleistocene, Rapolano Terme, Italy, *Sedimentology*, *45*(1), 163–180.
Halbach, B. K. (1980), Design of permanent multipole magnets with oriented rare earth cobalt materials, *Nucl. Instrum. Methods*, *169*, 1–10, doi:10.1016/0029.
Hassall, J. K., P. Ferraris, M. Al-Raisi, N. F. Hurley, A. Boyd, and D. F. Allen (2004), Comparison of permeability predictions from NMR, formation image and other logs in a carbonate reservoir, paper SPE 88683 present at the 11th Abu Dhabi International Petroleum Exhibition and Conference, Abu Dhabi Company for Onshore Oil Operations, Abu Dhabi, U.A.E., 10–13 Oct.
Hossain, Z., C. a. Grattoni, M. Solymar, and I. L. Fabricius (2011), Petrophysical properties of greensand as predicted from NMR measurements, *Pet. Geosci.*, *17*(2), 111–125, doi:10.1144/1354-079309-038.
Jones, B., and X. Peng (2012), Amorphous calcium carbonate associated with biofilms in hot spring deposits, *Sediment. Geol.*, *269-270*, 58–68, doi:10.1016/j.sedgeo.2012.05.019.
Kano, A., J. Matsuoka, T. Kojo, and H. Fujii (2003), Origin of annual laminations in tufa deposits, southwest Japan, *Palaeogeogr. Palaeoclimatol. Palaeoecol.*, *191*(2), 243–262, doi:10.1016/0031-0182(02)00717-4.
Kele, S., M. Özkul, I. Fórizs, A. Gökgöz, M. O. Baykara, M. C. Alçiçek, and T. Németh (2011), Stable isotope geochemical study of Pamukkale travertines: New evidences of low-temperature non-equilibrium calcite-water fractionation, *Sediment. Geol.*, *238*(1-2), 191–212, doi:10.1016/j.sedgeo.2011.04.015.
Madigan, M. T., J. M. Martinko, D. A. Stahl, and D. P. Clark (2012), *Brock Biology of Microorganisms*, 13th ed., Benjamin Cunnings, San Francisco.
Maliva, R. G., T. M. Missimer, E. a. Clayton, and J. a. D. Dickson (2009), Diagenesis and porosity preservation in Eocene microporous limestones, South Florida, USA, *Sediment. Geol.*, *217*(1-4), 85–94, doi:10.1016/j.sedgeo.2009.03.011.
Meiboom, S., and D. Gill (1958), Modified Spin-Echo Method for Measuring Nuclear Relaxation Times, *Rev. Sci. Instrum.*, *29*(8), 688–691, doi:10.1063/1.1716296.
Okumura, T., C. Takashima, F. Shiraishi, and A. Kano (2012), Textural transition in an aragonite travertine formed under various flow conditions at Pancuran Pitu, Central Java, Indonesia, *Sediment. Geol.*, *265–266*, 195–209, doi:10.1016/j.sedgeo.2012.04.010.
Özkul, M., S. Kele, A. Gökgöz, C.-C. Shen, B. Jones, M. O. Baykara, I. Fórizs, T. Németh, Y.-W. Chang, and M. C. Alçiçek (2013), Comparison of the Quaternary travertine sites in the Denizli extensional basin based on their depositional and geochemical data, *Sediment. Geol.*, *294*, 179–204, doi:10.1016/j.sedgeo.2013.05.018.
Pentecost, A. (2005), *Travertine*, Springer, Berlin.
Pentecost, A., S. Bayari, and C. Yesertener (1997), Phototrophic microorganisms of the Pamukkale travertine, Turkey: Their distribution and influence on travertine deposition, *Geomicrobiol. J.*, *14*, 269–283.
Rata, D. G., F. Casanova, J. Perlo, D. E. Demco, and B. Blümich (2006), Self-diffusion measurement by a mobile single-sided NMR sensor with improved magentic field gradient, *J. Magn. Reson.*, *180*(2), 229–235.
Ronchi, P., and F. Cruciani (2015), Continental carbonates as a hydrocarbon reservoir, an analog case study from the travertine of Saturnia, Italy, *AAPG Bull.*, *99*(04), 711–734, doi:10.1306/10021414026.
Rouquerol, F., J. Rouquerol, K. S. W. Sing, P. Llewellyn, and G. Maurin (2013), *Adsorption by Powders and Porous Solids*, 2nd ed., Academic Press.
Sharp, I. et al. (2013), Pre- and post-salt non-marine carbonates of the Namibe Basin, Angola, in *Microbial Carbonates in Space and Time: Implications for Global Exploration and Porduction*, pp. 52–53, Geol. Soc. of London, London, U. K.
Soete, J. (2016), Pore network characterization in complex carbonate systems-–A multidisciplinary approach, PhD dissertation, KU Leuven, Leuven, Belgium.
Soete, J., L. M. Kleipool, H. Claes, S. Claes, H. Hamaekers, S. Kele, M. Özkul, A. Foubert, J. J. G. Reijmer, and R. Swennen (2015), Acoustic properties in travertines and their relation to porosity and pore types, *Mar. Pet. Geol.*, *59*, 320–335, doi:10.1016/j.marpetgeo.2014.09.004.
Van Noten, K., H. Claes, J. Soete, A. Foubert, M. Özkul, and R. Swennen (2013), Fracture networks and strike–slip deformation along reactivated normal faults in Quaternary travertine deposits, Denizli Basin, western Turkey, *Tectonophysics*, *588*, 154–170, doi:10.1016/j.tecto.2012.12.018.
Veysey, J., B. W. Fouke, M. T. Kandianis, T. J. Schickel, R. W. Johnson, and N. Goldenfeld (2008), Reconstruction of water temperature, pH, and flux of ancient hot springs from travertine depositional facies, *J. Sediment. Res.*, *78*(2), 69–76, doi:10.2110/jsr.2008.013.
Vincent, B., M. Fleury, Y. Santerre, and B. Brigaud (2011), NMR relaxation of neritic carbonates: An integrated petrophysical and petrographical approach, *J. Appl. Geophys.*, *74*(1), 38–58, doi:10.1016/j.jappgeo.2011.03.002.
Volery, C., E. Davaud, C. Durlet, B. Clavel, J. Charollais, and B. Caline (2010), Microporous and tight limestones in the Urgonian Formation (late Hauterivian to early Aptian) of the French Jura Mountains: Focus on the factors controlling the formation of microporous facies, *Sediment. Geol.*, *230*(1-2), 21–34, doi:10.1016/j.sedgeo.2010.06.017.
Westphal, H., I. Surholt, C. Kiesl, H. F. Thern, and T. Kruspe (2005), NMR Measurements in Carbonate Rocks: Problems and an Approach to a Solution, *Pure Appl. Geophys.*, *162*(3), 549–570, doi:10.1007/s00024-004-2621-3.
Wright, P. V. (2012), Lacustrine carbonates in rift settings: The interaction of volcanic and microbial processes on carbonate deposition, *Geol. Soc. Spec. Publ.*, *370*(1), 1–39.
Zhang, C. L., B. W. Fouke, G. T. Bonheyo, A. D. Peacock, D. C. White, Y. Huang, and C. S. Romanek (2004), Lipid biomarkers and carbon-isotopes of modern travertine deposits (Yellowstone National Park, USA): Implications for biogeochemical dynamics in hot-spring systems, *Geochim. Cosmochim. Acta*, *68*(15), 3157–3169, doi:10.1016/j.gca.2004.03.005.
Zinszner, B., and F.-M. Pellerin (2007), *A Geoscientist's Guide to Petrophysics*, A Geoscientist's Guide to Petrophysics, edited by IFP Publications, 384 pp., Technip, Paris.